

Wavelet Spatio-Temporal Change Detection on multi-temporal SAR images

Rodney V. Fonseca , Rogério G. Negri , Aluísio Pinheiro , and Abdourrahmane Atto  *Senior Member, IEEE*

Abstract—We introduce WECS (Wavelet Energies Correlation Screening), an unsupervised procedure to detect spatio-temporal change points on multi-temporal SAR images. The procedure is based on wavelet approximation for the multi-temporal images, wavelet energy apportionment, and ultra-high dimensional correlation screening for the wavelet coefficients. We show WECS performance on simulated multi-temporal image data. We also evaluate the proposed method on a time series of 85 satellite images in a forest region at the border of Brazil and the French Guiana. The proposed method displays good results in covering change regions, with the additional benefit of having simple and fast computation.

Index Terms—Change detection, remote sensing, multi-temporal images, simulated images, wavelets.

I. INTRODUCTION

CHANGE detection is an important task performed in remote sensing image that allows researchers and engineers to identify and evaluate modifications on land surfaces captured by multi-temporal satellite images. Analyzing problems such as deforestation [1], rapid urbanization [2] and glacier melting [3] are of great importance to study the dynamics of regions sensitive to climate changes and human activity. Furthermore, the increase on availability of satellite images in the past years raises the challenge of applying computationally cheap methods to large images available over long periods. A review for change detection in multi-temporal remote sensing is given by [4].

Most methods used for change detection analysis can be classified either as supervised (training data is used to set up the method) or unsupervised (fully data-driven techniques). We focus in this work on unsupervised approaches, whose examples in the literature include the works of [5]–[10]. Many other proposals vary in their motivations as well as in their applicability. Change detection in multi-temporal hyperspectral images is discussed in [11]–[13]. [14] pursue change detection techniques via non-local means and principal component analysis. Compressed projection and image fusion are employed by [15]. Deep slow feature analysis for change detection is

This work was supported by FAPESP (grants 2016/24469-6, 2018/04654-9, 2021/01305-6 and 2021/04513-9) and CNPq (grants 309230/2017-9 and 310991/2020-0).

R. Fonseca and A. Pinheiro are with the Department of Statistics, University of Campinas, Campinas 13083-859, Brazil (e-mails: ra192588@dac.unicamp.br; pinheiro@ime.unicamp.br).

A. Atto is with the LISTIC - Polytech Annecy-Chambéry, Université de Savoie, 74944 Annecy le Vieux Cedex, France (e-mail: Abdourrahmane.Atto@univ-savoie.fr).

R. G. Negri is with the Department of Environmental Engineering, São Paulo State University, São José dos Campos, Brazil (e-mail: rogerio.negri@unesp.br).

the subject of [16]. [17] proposes a change detection method driven by adaptive parameter estimation.

A special attention has been given for multi-temporal change detection using Synthetic Aperture Radar (SAR) images. Some of the references already mentioned are examples of change detection methods applied to SAR images [1]–[3], [7], [14], [15]. Known to be unaffected by weather, cloud and sunlight conditions, SAR images rise as an essential data source in change detection applications [18]. Conversely, due to its acquisition architecture, the speckle noise typically affects the images obtained by SAR sensors and demands additional pre-processing before its use.

Change detection process using SAR images is a challenging task due to the high-dimensionality of multi-temporal datasets associated with the speckle noise. In this context, the use of Wavelets rises as a convenient approach given robustness when dealing with noise data and the available efficient computational algorithms.

Wavelet-based methods present many advantages for a plethora of statistical applications [19] thanks to wavelet capabilities in capturing multi-scale/resolution information. Their computational efficiency and sparseness are specially relevant for large images and other high-dimensional data [20]. SAR images have been investigated under different approaches using wavelet methods [21]–[24]. On the other hand, there are variable selection methods that have been successfully applied in high-dimensional statistical models but that are still novel ideas in the wavelet and change detection literature. We show that one of these methods has an interesting potential to provide good results even with simple algorithms.

Given the aforementioned discussion and motivation, we propose the Wavelet Energies Correlation Screening (WECS), a novel unsupervised multi-temporal change detection method for SAR images. The main idea behind WECS is built on ultra-high dimensional feature screening for the wavelet coefficients [25]. Such method is usually employed in high-dimensional regression models to reduce the problem's dimension by subsetting the available covariates in such a way that true covariates are among the chosen ones with high probability [26]. We show that by applying the feature screening idea on multi-temporal images, we obtain a fast and accurate method to cover change regions with good detection rates.

This paper is organized as follows: basic concepts and definitions are presented in Section II. Section III introduces the problem and presents the proposed method. We show WECS performance on simulated multi-temporal image data in Section IV-B. In Section IV-C we apply the proposed method to a time

series of 85 satellite images in the border region of Brazil and the French Guiana, for images captured from December 26th 2015 to December 3rd 2017. Section V concludes this study.

II. BASIC THEORY BACKGROUND

Wavelet methods have been widely applied to analyze images in signal processing literature, specially for tasks such as signal denoising and compression [27]. The most common way of describing wavelet representations is as a multi-resolution decomposition, where a signal is represented on approximation and detail coefficients, which provide coarse and finer details of the signal, respectively. In practice, the discrete wavelet transform of matrices (image) consists in applying low and high-pass convolution filters to its rows and columns [28]. In case of smoothing, applying such low-pass filter J times to rows and columns of a matrix \mathcal{I} , yields a smooth image \mathbf{X} . The number J is also called resolution level, a tuning parameter for wavelet smoothing.

Although the wavelet smoothing on images embraces an initial step to analyze the data, the main goal is to find the spatial changes over time. The smoothed images still contain many coefficients that need to be evaluated simultaneously, which characterizes a high-dimensional problem with multiple time series corresponding to each location in space. Consequently, retaining only the most essential locations driving overall modifications across time is desirable. This issue is recurrent in regression analysis when selecting the most relevant variables. The feature screening technique is a particularly efficient method to identify relevant variables, especially when the number of candidates is large.

Feature screening is a method originally designed for high and ultra-high dimensional regression models [26]. Consider the usual linear regression framework where \mathbf{y} is a $n \times 1$ vector of observations from a response variable and $\{\mathbf{W}_1 \cdots \mathbf{W}_p\}$ is a $n \times p$ matrix with explanatory variables on its columns, which are used in a linear model $\mathbf{y} = \sum_{i=1}^p \beta_i \mathbf{W}_i + \boldsymbol{\epsilon}$, β_1, \dots, β_p are unknown parameters and $\boldsymbol{\epsilon}$ is a zero mean random noise. The problem setup is such that p is much larger than n , which makes standard regression methods unfeasible. Moreover, only a handful of the available covariates are relevant for the model, i.e., have a nonzero corresponding parameter β_i . The feature screening idea consists in computing the sample correlation $\text{corr}(\mathbf{y}, \mathbf{W}_i)$ among response and explanatory variables, and then selecting those covariates whose correlation are among the highest values. Under suitable conditions, such method is known to select a set containing all true covariates with high probability. In the image change detection problem, our idea is that a similar approach should be used to detect change locations by taking an overall change measure as response variable and local (pixel) measures as potential covariates.

III. WAVELET ENERGY CORRELATION SCREENING

Figure 1 depicts a high-level conceptualization for the proposed method. The elements included in such representation are formalized in the constructions as follows.

Let $\mathcal{I}^{(1)}, \dots, \mathcal{I}^{(n)}$ be an image time series defined on a support $\mathcal{S} = \{1, \dots, u\} \times \{1, \dots, v\} \subset \mathbb{N}^2$, hence representing

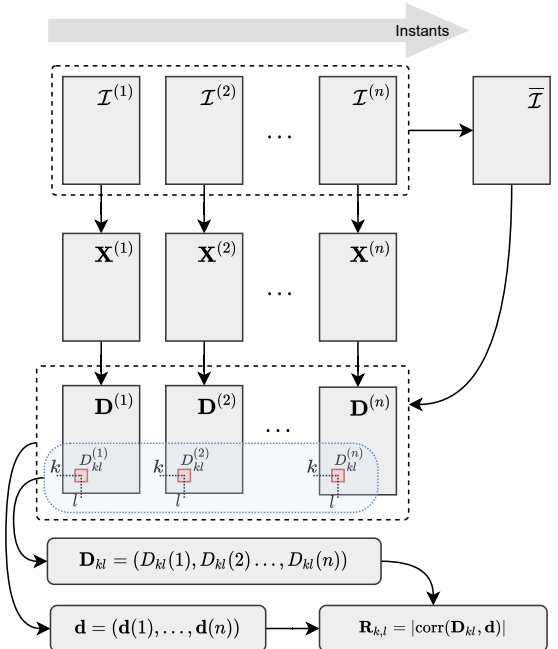


Fig. 1. Diagram of steps performed on WECS to compute an absolute correlation of a single point.

a region of interest over n distinct instants. Such images are relative to one SAR channel or a combination of channels; this will be specified when appropriate. Our goal is twofold: to find possible points in time where some relevant changes might have taken place at the region represented in $\mathcal{I}^{(m)}$, $m = 1, \dots, n$, and to find which regions are closely associated to the observed changes over time. We shall address these tasks by analyzing the bidimensional stationary discrete wavelet decomposition of $\mathcal{I}^{(m)}$. Stationary wavelets (also known as non-decimated or redundant wavelets) is a traditional de-noising method that can be efficiently applied to two-dimensional signals such as images [21], [29], [30].

The application of this wavelet transform to $\mathcal{I}^{(m)}$ at some appropriate resolution level $J \geq 1$ results in a matrix of the so called approximation wavelet coefficients $\mathbf{X}^{(m)}$ of $\mathcal{I}^{(m)}$ defined on the same support \mathcal{S} . The higher $J \in \{1, 2, \dots, \lfloor \log_2(\min\{u, v\}) \rfloor\}$ is, the smoother $\mathbf{X}^{(m)}$ gets.

Beyond many other aspects that are involved in wavelet analyses of images, which may include different wavelet bases as well as the use of thresholding of detail coefficients, the current construction is focused on $\mathbf{X}^{(m)}$ to provide a simple wavelet smoothing. Nevertheless, extensions based on distinct aspects are straightforward.

We can then consider further apportioning the total \mathbb{L}_2 energy of the series $\left\{\mathbf{X}^{(m)}\right\}_{m=1}^n$ as:

$$\begin{aligned} \sum_{m=1}^n \|\mathbf{X}^{(m)}\|_F^2 &= n\|\bar{\mathcal{I}}\|_F^2 + 2n\langle \bar{\mathbf{X}} - \bar{\mathcal{I}}, \bar{\mathcal{I}} \rangle_F + \\ &\quad + \sum_{m=1}^n \|\mathbf{X}^{(m)} - \bar{\mathcal{I}}\|_F^2, \end{aligned} \tag{1}$$

where $\bar{\mathcal{I}} = n^{-1} \sum_{m=1}^n \mathcal{I}^{(m)}$ and $\bar{\mathbf{X}} = n^{-1} \sum_{m=1}^n \mathbf{X}^{(m)}$; $\|\cdot\|_F$

and $\langle \cdot, \cdot \rangle_F$ represents the Frobenius norm and inner product, respectively. Naturally, both $\bar{\mathcal{I}}$ and $\bar{\mathbf{X}}$ share the support \mathcal{S} .

The last term on the right-hand side of Equation (1) measures the deviations between the wavelet coefficients at distinct instants ($\mathbf{X}^{(m)}$; $m = 1, \dots, n$) and the *average image* (i.e., $\bar{\mathcal{I}}$). Such deviations may favor detecting relevant changes over time. Since each element (i.e., a pixel/position $(k, l) \in \mathcal{S}$) of $\mathbf{X}^{(m)}$ also has a corresponding sequence of deviations in time, the local deviation to the overall measure may also allow detecting spatial changes. Among several approaches able to detect change events, the Pearson correlation coefficient is an interesting alternative. Furthermore, such measure shares connections with the idea of feature screening employed in high-dimensional regression [26].

Let $X_{kl}^{(m)}$ and \bar{I}_{kl} be the entry (k, l) of $\mathbf{X}^{(m)}$ and $\bar{\mathcal{I}}$, respectively. The matrix $\mathbf{D}^{(m)}$ embraces the squared differences between $\mathbf{X}^{(m)}$ and $\bar{\mathcal{I}}$, where $D_{kl}^{(m)} = (\mathbf{X}_{kl}^{(m)} - \bar{I}_{kl})^2$. Therefore, the temporal overall variation sequence is defined as $\{\mathbf{d}^{(m)}\}_{m=1,\dots,n}$, whose elements are given by:

$$\mathbf{d}^{(m)} = \sum_{k=1}^u \sum_{l=1}^v D_{kl}^{(m)}. \quad (2)$$

In this context, an instant m in $\{\mathbf{d}^{(m)}\}_{m=1,\dots,n}$ with high value stands for the image $\mathcal{I}^{(m)}$ where the most expressive changes take place.

In order to identify spatio-temporal changes, we employ the concept of ultra-high dimensional correlation screening [25] discussed in Section II. For each local squared deviation time series given by individual elements of $\mathbf{D}^{(m)}$ across $m = 1, \dots, n$, say $\mathbf{D}_{kl} = \{D_{kl}^{(1)}, \dots, D_{kl}^{(n)}\}$, consider the absolute value of its Pearson correlation with the overall squared deviations \mathbf{d} :

$$R_{kl} = |\text{corr}(\mathbf{D}_{kl}, \mathbf{d})|. \quad (3)$$

Consequently, it is defined $\mathbf{R} = \{R_{kl}\}$ as the matrix of absolute correlations, where R_{kl} is assigned to each $(k, l) \in \mathcal{S}$.

Define a mapping of *relevant* indices for changes over the image series with respect to $\bar{\mathcal{I}}$ as $\mathcal{M}^* \subseteq \mathcal{S}$ where *changes in $\{\mathcal{I}^{(m)}\}_{m=1,\dots,n}$ with respect to $\bar{\mathcal{I}}$ are affected by local changes in the images*.

If we apply to Equation (2) the index dichotomy defined by \mathcal{M}^* , we have

$$\mathbf{d}^{(m)} = \sum_{(k,l)} \beta_{kl} D_{kl}^{(m)} + \varepsilon^{(m)}, \quad (4)$$

where β_{kl} are non-null regression coefficients for $(k, l) \in \mathcal{M}^*$, and $\varepsilon^{(m)}$ are stochastic error terms. The error terms allow for both the apportionment of spurious correlation for indices not in \mathcal{M}^* as well as for the energies not represented by the wavelet smoothing.

It is a well-known property of discrete wavelet transforms that it statistically decorrelates the original data [19], [20]. For instance, this motivates the use of WECS instead of a non-wavelet version of energy correlation, since wavelets will result in sparser representations for \mathcal{M}^* . Moreover, the sure screening

theoretical results for independent data motivates our conjecture that the regression set-up given by Equation (4) should have a good performance. A rigorous proof for dependent data sets such as multitemporal series of satellite images is beyond the scope of this manuscript, but the numerical results provide us with some solid evidences.

Finally, an empirical mapping of change locations may be stated as:

$$\mathcal{M}_\tau = \{(k, l) \in \mathcal{S} : |R_{kl}| > \tau\}, \quad (5)$$

where $\tau \in \mathbb{R}_+^*$ is a convenient threshold value. The idea is that, for suitable values of τ , the empirical set \mathcal{M}_τ has high probability of detecting the correct change locations in \mathcal{M}^* [25].

IV. EXPERIMENTS

A. Experimental design

In order to assess the proposed method's performance, this section presents two studies comprising distinct datasets.

The first study (Sec. IV-B) uses a simulated data set and focus on identifying the most appropriate wavelet family and resolution level J . Specifically, the Haar (haar), Daubechies of order 2 and 4 (db2 and db4), Coiflets of order 4 (coif4) and Symlets of order 2 and 4 (sym2 and sym4) wavelet families are analyzed [31], [32]. The performance of the proposed method is measured in terms of True/False Positive Ratios and Receiver Operating Characteristic (ROC) curve.

Comparisons with the standard Thresholding of Aggregate Absolute Difference (TAAD) and a non-wavelet version of WECS, herein called Energy Correlation Screening (ECS), are included in the experiments. In summary, the TAAD comprises the application of a thresholding algorithm on the accumulated change representation image \mathbf{A} where $A_{kl} = \sum_{m=2}^n |\mathcal{I}_{kl}^{(m)} - \mathcal{I}_{kl}^{(m-1)}|$. The ECS stands for the use of $\mathcal{I}^{(m)}$ instead of $\mathbf{X}^{(m)}$ when defining $D_{kl}^{(m)}$ at Equation 2, and consequently Equation 3. The resulting “Pearson correlation” matrix from ECS approach is denoted by $\tilde{\mathbf{R}}$.

The second study (Sec. IV-C) presents an analysis on the performance of WECS, and respective comparison with TAAD and ECS, in a real-world application with actual SAR image series. The appropriate wavelet family and resolution level previously identified are employed. F1-Score [33], True/False Positive/Negative (TP, TN, FP and FN) rates, the kappa coefficient, and the variance of kappa [34], are adopted for this purpose. Additionally, the computational run-times are presented and discussed.

We used a computer with an Intel Intel i-7 processor (8 core, 3.5 GHz), and 16 GB of RAM running the Ubuntu Linux version 20.04 operating system. The code of the proposed method is freely available at <https://github.com/rodneyfv/wecs>.

B. Simulated data analysis

We discuss here the application of WECS, TAAD, and ECS on a simulated multi-temporal image dataset. Such series comprises 80 multi-temporal images and it is synthesized by repeating a sequence of four images with different types of changes plus noise. Examples of the first four time instants

are shown in Figure 2. These images/instants are generated by summing two matrices: (i) a binary signal matrix with ones denoting where the ellipses occur and zero elsewhere; (ii) and a noise matrix with random variables following a standard Gaussian distribution.

The first image, $\mathcal{I}^{(1)}$, presents three elongated ellipses. The second image $\mathcal{I}^{(2)}$ has shorter and larger ellipses added. Smaller ellipses are then added to form $\mathcal{I}^{(3)}$ and $\mathcal{I}^{(4)}$. Patterns of changes between subsequent images are shown in Figure 3(a), where white regions (i.e., “ones”) correspond to changes.

Applying WECS to these images we obtain a matrix \mathbf{R} of correlations between deviations of each \mathcal{I} entry with the total squared mean deviation. A typical example of \mathbf{R} is presented in Figure 3(b). For some choice of threshold τ on absolute values of \mathbf{R} , we obtain a binary matrix that can be compared with the total true changes shown in Figure 3(a). Similarly, Figures 3(c) and 3(d) depict the matrices \mathbf{A} and $\tilde{\mathbf{R}}$ provided by TAAD and ECS methods.

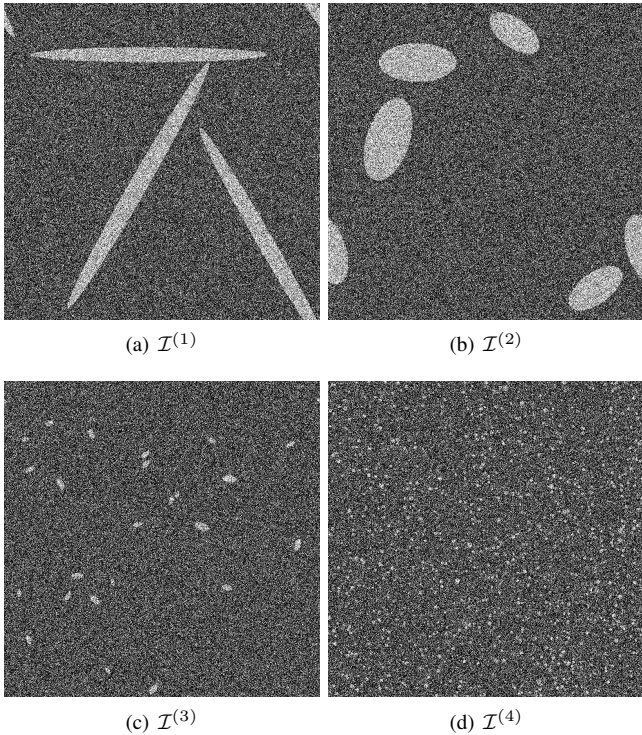


Fig. 2. Example of the first four simulated multi-temporal images. Features and changes come as white ellipses and dots.

According to the experimental design (Section IV-A), ROC curves are employed to compare the performance of each analyzed method and inspect the effects of both J and wavelet basis on the performance of the WECS method. In summary, the ROC curves exhibit the performance as a function of true and false positive ratios when distinguishing two events (in this context, the change and no-change pixels/positions) using distinct thresholds. The true and false positive ratios are computed using the “total change” image (Fig. 3(a)) as reference. Moreover, the tested thresholds embrace all values in \mathbf{R} (or \mathbf{A}), excluding repetitions and considering it in ascending order.

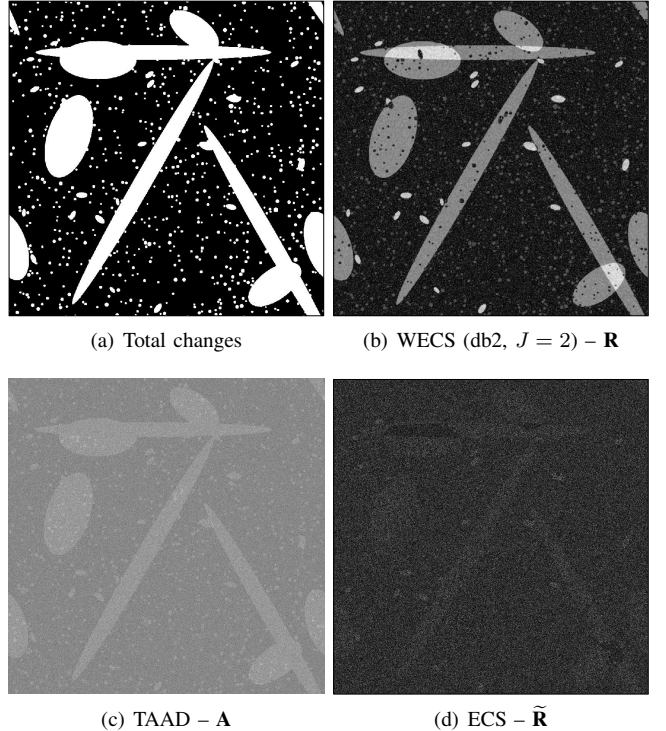


Fig. 3. Expected change/non-change regions and typical results provided by WECS, TAAD and ECS before the thresholding process.

Figure 4(a) presents the ROC curves considering different wavelet bases in the WECS method. All instances adopt $J = 2$. We conclude that db2 and sym2 deliver the best trade-off between true and false positive ratios (i.e., high true positive ratios even when the false positive ratios are low). As a consequence of this finding, all the following experiments and analyses consider the db2 wavelet basis.

Figure 4(b) depicts the ROC curves with $J \in \{1, 2, 3, 4, 5\}$ as decomposition levels. The profiles exhibited by the ROC curves provide evidences that J equal to 2 or 3 lead to the best performances. $J = 2$ has a slight advantage, since it demands fewer decomposition levels. The overall performance for $J = 2$ warrants its use for the rest of the comparisons.

The ROC curves shown in Figure 4(c) present the performances of WECS, TAAD and ECS. ECS’s low performance shows that the simple swap of the wavelet transform by a “deviation image” into the proposed correlation screening pipeline is an inconvenient choice and reinforces the importance of the wavelet smoothing in the context of the proposed method. Regarding TAAD’s performance, a True Positive Ratio of 0.8 is guaranteed when tolerating a False Positive Ratio of approximately 0.4. Since WECS provides the same True Positive Ratio under an almost nil false positive ratio, its superior performance is clearly established.

C. Actual remote sensing application

This section compares the performance of WECS, TAAD and ECS in a real-world change detection application. The appropriate wavelet basis and resolution level previously identified in Section IV-B (i.e., db2 and $J = 2$) are employed.

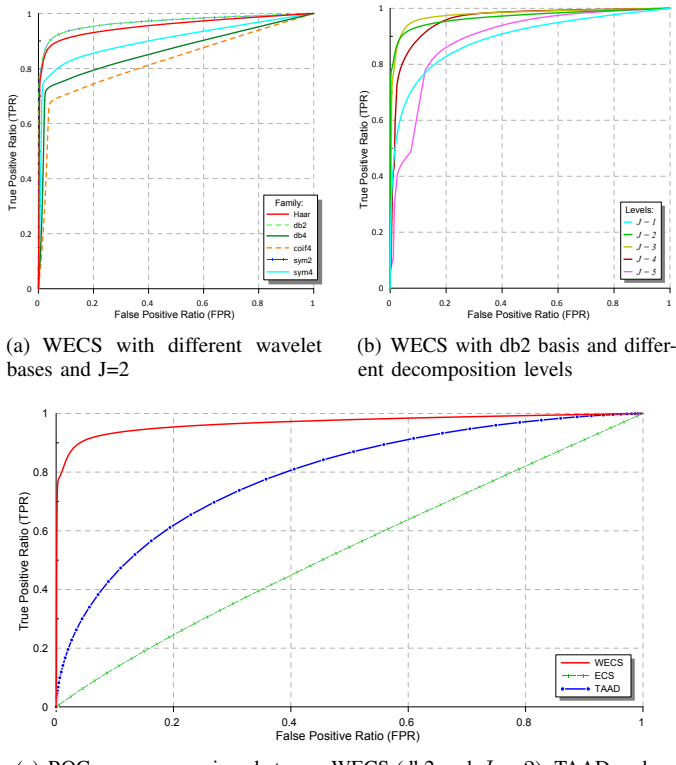


Fig. 4. ROC curves related to the experiment with simulated dataset.

We consider here a large multi-temporal series of 85 images acquired over a forest region at the border of Brazil and the French Guiana (Fig. 5), from December 26th 2015 to December 3rd 2017, by the SAR sensor onboard the Sentinel-1 satellite.

Each image contains the amplitude signal backscatters relative to VV and VH polarizations, a spatial resolution of 10 m and a support of 1538×1556 pixels wide in ground range projection. Specifically, these images were obtained from the *Sentinel-1 SAR GRD* dataset maintained by the European Space Agency [35]. Figures 6(a) and 6(b) depict the first and last images of the time series, where it is possible to compare and identify some landscape changes.

After careful visual inspection of the backscatter profile of each image in the series, it is possible to identify the regions where the land cover change occurs or does not occur, allowing then collecting reference samples regarding the “change” and “non-change” conditions. Such samples are needed to compute the accuracy measures beforehand mentioned in Section IV-A. The spatial distribution of these samples is presented in Figure 6(c).

In order to apply the analyzed methods, the dual-polarized images were combined into a single-band representation considering the so-called “span” image $\mathcal{I}_{kl}^{(m)} = \sqrt{(\text{VV}_{kl}^{(m)})^2 + (\text{VH}_{kl}^{(m)})^2}$, with VV and VH representing the available polarizations.

Initially, to express the instantaneous change values with respect to WECS, Figure 7 presents the temporal variations given by \mathbf{d} . According to the presented profile, it is possible

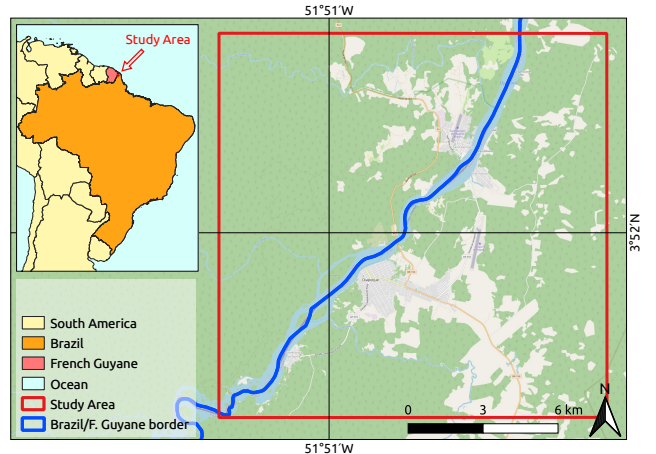


Fig. 5. The study area location.

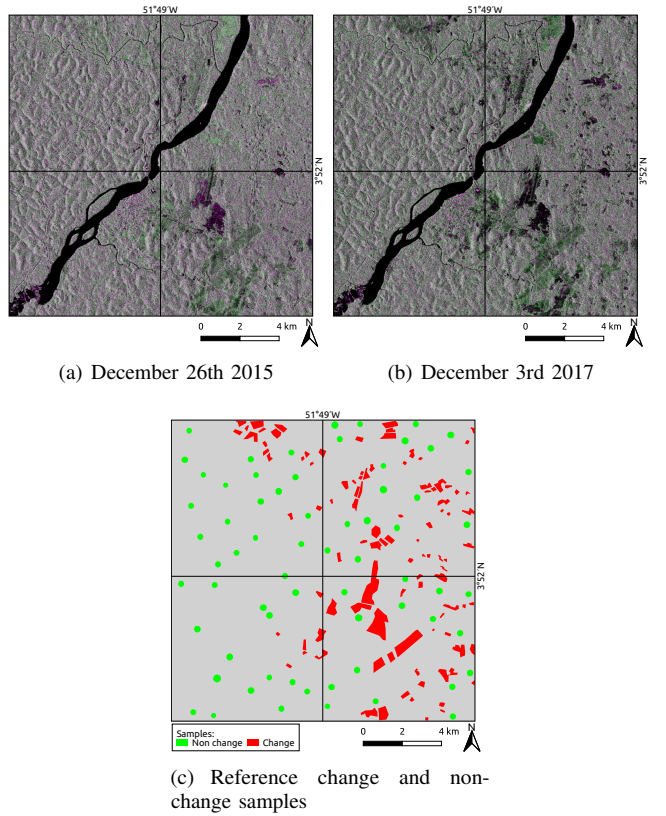


Fig. 6. First and last images in the adopted multitemporal image series, in VV-HV-VV RGB color composition, and reference samples.

to observe the fluctuations around a central value near 12 as highlight instants with a value similar, higher or lower than this baseline, as pointed out for m equal to 1, 30 and 59, respectively. For the sake of comparison, the wavelet representation at each mentioned instant (i.e., $\mathbf{X}^{(1)}$, $\mathbf{X}^{(30)}$ and $\mathbf{X}^{(59)}$) and the mean image (i.e., $\bar{\mathbf{I}}$) are exhibited in Figure 8. While $\mathbf{X}^{(1)}$ shares similarities with $\bar{\mathbf{I}}$, evident changes increase in $\mathbf{X}^{(30)}$. Reversely, $\mathbf{X}^{(59)}$ offers low contribution for identifying change regions.

Through the application WECS, ECS and TAAD to the image series, we obtain matrices \mathbf{R} , $\tilde{\mathbf{R}}$ and \mathbf{A} . They represent the

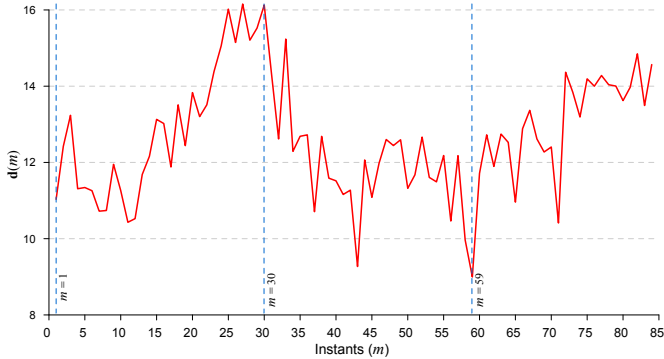


Fig. 7. Plot of $d(m)$ for $m = 1, \dots, 85$. Distinct deviations occur at $m = 1$ (intermediate), 30 (high) and 59 (low). Baseline around 12.

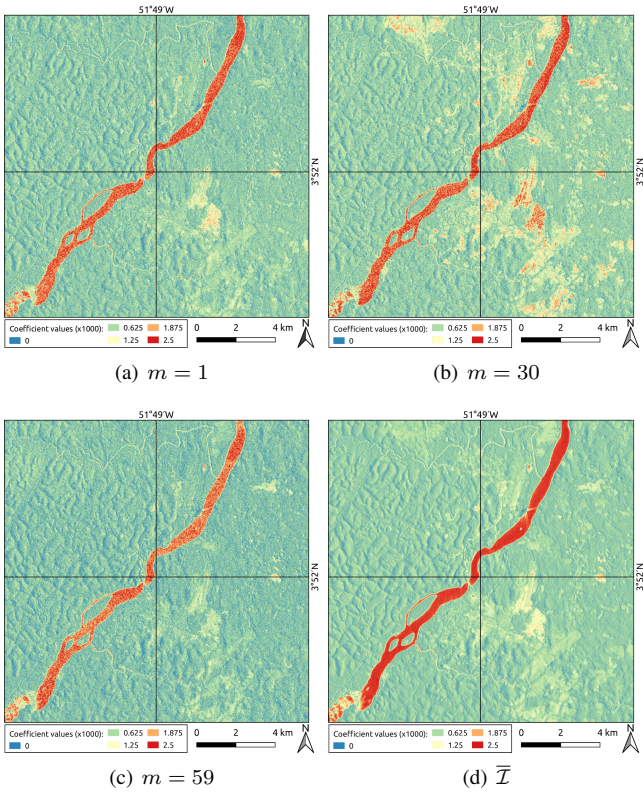


Fig. 8. Images $\mathbf{X}^{(m)}$ for $m = 1, 30, 59$ and mean image $\bar{\mathbf{I}}$.

spatially-localized change measures given by WECS, ECS and TAAD, respectively. Such matrices are presented in Figure 9, where high values stand for regions with changes in their land cover over time. However, to determine a cut-off value τ for such matrices, providing then binary maps \mathcal{M}_τ of “change” and “non-change” areas (Equation 5), the use of thresholding techniques rises as a convenient procedure. Among different alternatives in the literature, the Otsu (OT) [36] and Kittler-Illingworth (KI) [37] thresholding techniques had been successfully employed for change detection purposes [9], [38]–[40].

The accuracy of the binary maps \mathcal{M}_τ , resulting from the application of OT and KI algorithms on the change images

provided by WECS, ECS and TAAD, are measured in terms of the F1-Score and the kappa coefficient based on the reference ground-truth samples (Fig. 6(c)). Table I presents the computed accuracy measures.

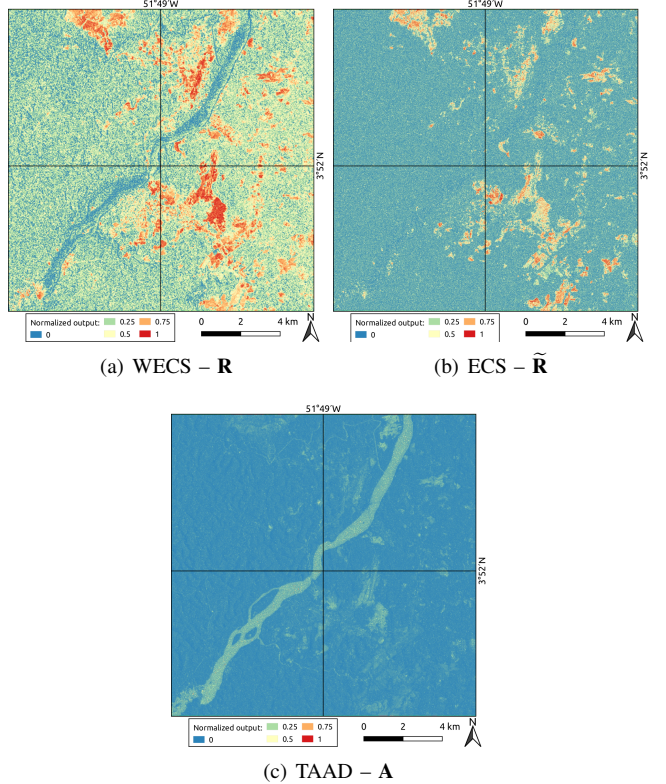


Fig. 9. The “tendency of change” matrices \mathbf{R} , $\tilde{\mathbf{R}}$ and \mathbf{A} assigned to WECS, ECS and TAAD, respectively. The values are scaled to $[0, 1]$.

According to the adopted accuracy measures, WECS, especially when submitted to the OT algorithm, presents a better performance detecting change locations without increasing/inflating the amount of false positives (FP), which is justified by a higher F1-Score level in comparison to the competitors ECS and TAAD. Moreover, according to the kappa coefficient, WECS also delivers a more balanced correct classification regarding the change and non-change areas. Furthermore, based on the kappa values and respective variances, it is verified that the difference between any pair of results is significant at 1%.

Although WECS’s performance when equipped with the KI algorithm is inferior to the OT algorithm, it is worth observing that the introduced methods still provide more accurate results than either ECS or TAAD. Regarding the competitors, TAAD presents frequent FP errors, leading to lower F1-Score and kappa coefficient than ECS.

Figure 10 depicts the most accurate change/non-change maps according to the measures in Table I. It is possible to verify that, while TAAD-K1 assigns the water body as a “region of change”, it does not detect locations that changed (northwest and southeast portions – second and fourth quadrants). Regarding ECS, its result has a noise-corrupt character, with frequent FP classification points.

As previously observed, WECS equipped with the KI algorithm provides a homogeneous mapping over the non-change areas (west portion – second and third quadrants), accurate detection over the change regions, and low inclusion (FP) and exclusion (FN) error rates. In adopting the OT algorithm, the inclusion error increases, resulting in a less-regularized change/non-change map.

The proportions of True/False Positive/Negative assigned to the analyzed methods are shown in Figure 11 and corroborate the aforementioned discussion.

TABLE I
ACCURACY VALUES SUMMARY. VARIANCE OF KAPPA MULTIPLIED BY $\times 10^5$.

Threshold	WECS		ECS		TAAD	
	OT	KI	OT	KI	OT	KI
F1-Score	0.940	0.876	0.6189	0.661	0.798	0.778
Kappa	0.818	0.698	0.535	0.513	0.244	0.284
Var. of kappa	6.90	3.43	1.91	1.72	0.76	0.91

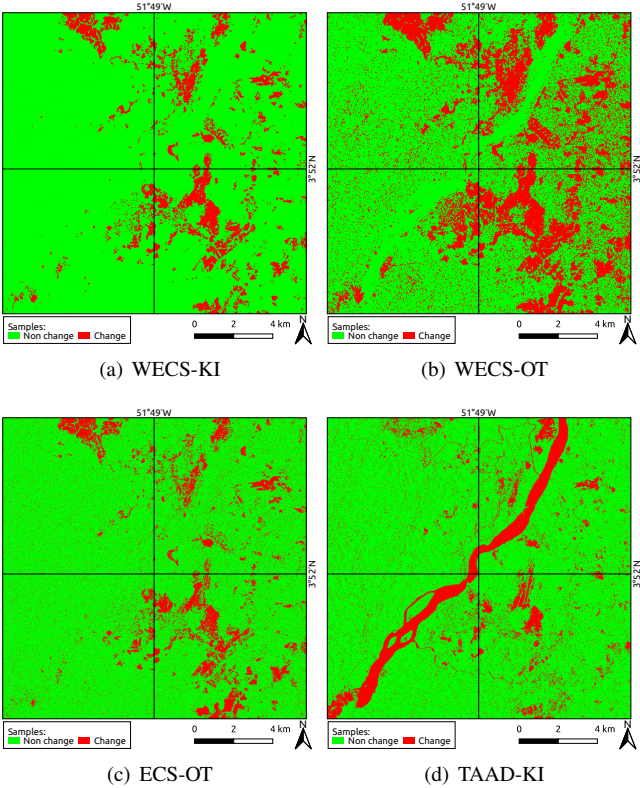


Fig. 10. Resulting change maps from the analyzed methods.

Lastly, the computational run-time of WECS, TAAD and ECS were, respectively, 143.45 s, 7.89 s and 110.08 s. Despite expending a longer execution time, it is worth mention that WECS' running time is not excessive in the context of remote sensing image processing, beyond providing systematically more accurate results.

V. CONCLUSION

We present a novel way of detecting changes in multi-temporal satellite images called WECS. The procedure is based on wavelet energies from both the estimated individual

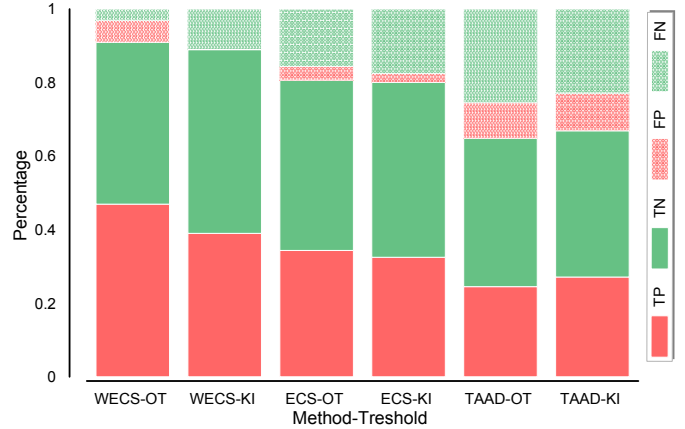


Fig. 11. Percentages of True/False Positives (TP/FP) and True/False Negatives (TN/FN) relative to change (Positive) and non-change (Negative) reference samples.

coefficients as well as the whole mean image. It makes use of correlation screening for ultra-high dimensional data to identify which locations (pixels) are the most related to an overall change measure of the image time series. Thereupon, WECS is expected to provide a sample of points in space in a way that such set contains real change points with high probability.

The performance of WECS was evaluated in studies involving simulated and real data. In both experiments, WECS is compared with two standard approaches for analyzing multi-temporal images. One drawback of WECS compared to standard methods is that it takes longer time to process the images. However, its performance is shown to be superior on both real and simulated image, and the processing time is still not prohibitive.

The current paper warrants future research in different directions, for example: adapting the idea of WECS to different types of images (multispectral, polarimetric SAR, etc); extending energy correlation screening for distinct smoothing techniques; deducing sharp theoretical change detection rates for appropriate statistical models.

ACKNOWLEDGMENT

The authors would like to thank the European Space Agency (ESA) for providing the Sentinel-1 data used in this research.

REFERENCES

- [1] T. L. Barreto, R. A. Rosa, C. Wimmer, J. B. Nogueira, J. Almeida, and F. A. M. Cappabianco, "Deforestation change detection using high-resolution multi-temporal X-band SAR images and supervised learning classification," in *2016 IEEE International Geoscience and Remote Sensing Symposium (IGARSS)*. Beijing, China: IEEE, 2016, pp. 5201–5204.
- [2] Y. Ban and O. A. Yousif, "Multitemporal spaceborne SAR data for urban change detection in China," *IEEE Journal of Selected Topics in Applied Earth Observations and Remote Sensing*, vol. 5, no. 4, pp. 1087–1094, 2012.
- [3] C. Scher, N. C. Steiner, and K. C. McDonald, "Mapping seasonal glacier melt across the Hindu Kush Himalaya with time series synthetic aperture radar (SAR)," *The Cryosphere*, vol. 15, no. 9, pp. 4465–4482, 2021.

- [4] Y. Ban and O. Yousif, "Change detection techniques: A review," in *Multitemporal Remote Sensing*, Y. Ban, Ed. Cham: Springer, 2016, pp. 19–43.
- [5] L. Bruzzone and D. F. Prieto, "Automatic analysis of the difference image for unsupervised change detection," *IEEE Transactions on Geoscience and Remote Sensing*, vol. 38, no. 3, pp. 1171–1182, 2000.
- [6] T. Celik, "Change detection in satellite images using a genetic algorithm approach," *IEEE Geoscience and Remote Sensing Letters*, vol. 7, no. 2, pp. 386–390, 2010.
- [7] G. Quin, B. Pinel-Puyssegur, J.-M. Nicolas, and P. Loreaux, "MIMOSA: An automatic change detection method for SAR time series," *IEEE Transactions on Geoscience and Remote Sensing*, vol. 52, no. 9, pp. 5349–5363, 2014.
- [8] S. Saha, F. Bovolo, and L. Bruzzone, "Change detection in image time-series using unsupervised LSTM," *IEEE Geoscience and Remote Sensing Letters*, 2020.
- [9] R. G. Negri, A. C. Frery, W. Casaca, S. Azevedo, M. A. Dias, E. A. Silva, and E. H. Alcântara, "Spectral-spatial-aware unsupervised change detection with stochastic distances and support vector machines," *IEEE Transactions on Geoscience and Remote Sensing*, vol. 59, no. 4, pp. 2863–2876, 2021.
- [10] R. G. Negri and A. C. Frery, "Unsupervised change detection driven by floating references: A pattern analysis approach," *Pattern Analysis and Applications*, vol. 24, pp. 933–949, 2021.
- [11] F. Bovolo and L. Bruzzone, "The time variable in data fusion: A change detection perspective," *IEEE Geoscience and Remote Sensing Magazine*, vol. 3, no. 3, pp. 8–26, 2015.
- [12] S. Liu, D. Marinelli, L. Bruzzone, and F. Bovolo, "A review of change detection in multitemporal hyperspectral images: Current techniques, applications, and challenges," *IEEE Geoscience and Remote Sensing Magazine*, vol. 7, no. 2, pp. 140–158, 2019.
- [13] T. Matsunaga, A. Iwasaki, S. Tsuchida, K. Iwao, J. Tanii, O. Kashimura, R. Nakamura, H. Yamamoto, S. Kato, K. Obata, K. Mouri, and T. Tachikawa, "Current status of hyperspectral imager suite (HISUI) onboard International Space Station (ISS)," in *2017 IEEE International Geoscience and Remote Sensing Symposium (IGARSS)*. Fort Worth, USA: IEEE, 2017, pp. 443–446.
- [14] M. Jia and L. Wang, "Novel class-relativity non-local means with principal component analysis for multitemporal SAR image change detection," *International Journal of Remote Sensing*, vol. 39, no. 4, pp. 1068–1091, 2018.
- [15] B. Hou, Q. Wei, Y. Zheng, and S. Wang, "Unsupervised change detection in SAR image based on Gauss-log ratio image fusion and compressed projection," *IEEE Journal of Selected Topics in Applied Earth Observations and Remote Sensing*, vol. 7, no. 8, pp. 3297–3317, 2014.
- [16] B. Du, L. Ru, C. Wu, and L. Zhang, "Unsupervised deep slow feature analysis for change detection in multi-temporal remote sensing images," *IEEE Transactions on Geoscience and Remote Sensing*, vol. 57, no. 12, pp. 9976–9992, 2019.
- [17] Y. Chen, Z. Ming, and M. Menenti, "Change detection algorithm for multitemporal remote sensing images based on adaptive parameter estimation," *IEEE Access*, vol. 8, pp. 106083–106096, 2020.
- [18] F. Bovolo and L. Bruzzone, "A detail-preserving scale-driven approach to change detection in multitemporal SAR images," *IEEE Transactions on Geoscience and Remote Sensing*, vol. 43, no. 12, pp. 2963–2972, 2005.
- [19] B. Vidakovic, *Statistical Modeling by Wavelets*. New York: John Wiley & Sons, 1999.
- [20] P. A. Morettin, A. Pinheiro, and B. Vidakovic, *Wavelets in Functional Data Analysis*. Cham: Springer, 2017.
- [21] A. M. Atto, E. Trouvé, Y. Berthoumieu, and G. Mercier, "Multidate divergence matrices for the analysis of SAR image time series," *IEEE Transactions on Geoscience and Remote Sensing*, vol. 51, no. 4, pp. 1922–1938, 2012.
- [22] N. Bouhel, G. Ginolhac, E. Jolibois, and A. Atto, "Multivariate statistical modeling for multi-temporal SAR change detection using wavelet transforms," in *2015 8th International Workshop on the Analysis of Multitemporal Remote Sensing Images (Multi-Temp)*. Annecy, France: IEEE, 2015, pp. 1–4.
- [23] T. Celik, "Multiscale change detection in multitemporal satellite images," *IEEE Geoscience and Remote Sensing Letters*, vol. 6, no. 4, pp. 820–824, 2009.
- [24] S. Cui and M. Datcu, "Statistical wavelet subband modeling for multi-temporal SAR change detection," *IEEE Journal of Selected Topics in Applied Earth Observations and Remote Sensing*, vol. 5, no. 4, pp. 1095–1109, 2012.
- [25] J. Fan, R. Li, C.-H. Zhang, and H. Zou, *Statistical Foundations of Data Science*. Boca Raton: CRC Press, 2020.
- [26] J. Fan and J. Lv, "Sure independence screening for ultrahigh dimensional feature space," *Journal of the Royal Statistical Society: Series B*, vol. 70, no. 5, pp. 849–911, 2008.
- [27] S. G. Mallat, *A Wavelet Tour of Signal Processing*. San Diego: Academic Press, 1998.
- [28] ———, "A theory for multiresolution signal decomposition: the wavelet representation," *IEEE transactions on pattern analysis and machine intelligence*, vol. 11, no. 7, pp. 674–693, 1989.
- [29] R. R. Coifman and D. L. Donoho, "Translation-invariant de-noising," in *Wavelets and statistics*, A. Antoniadis and G. Oppenheim, Eds. New York: Springer, 1995, pp. 125–150.
- [30] A. M. Atto, E. Trouvé, J.-M. Nicolas, and T. T. Lê, "Wavelet operators and multiplicative observation models—application to SAR image time-series analysis," *IEEE Transactions on Geoscience and Remote Sensing*, vol. 54, no. 11, pp. 6606–6624, 2016.
- [31] G. Beylkin, R. Coifman, and V. Rokhlin, "Fast wavelet transforms and numerical algorithms i," *Communications on Pure and Applied Mathematics*, vol. 44, no. 2, pp. 141–183, 1991.
- [32] I. Daubechies, *Ten Lectures on Wavelets*. USA: Society for Industrial and Applied Mathematics, 1992.
- [33] C. J. V. Rijsbergen, *Information Retrieval*, 2nd ed. USA: Butterworth-Heinemann, 1979.
- [34] R. G. Congalton and K. Green, *Assessing the accuracy of remotely sensed data: principles and practices*, 3rd ed. CRC press, 2019.
- [35] ESA, "European space agency – Sentinel-1 SAR Technical Guide." 2021, accessed: 2021-09-01. [Online]. Available: <https://sentinel.esa.int/web/sentinel/technical-guides/sentinel-1-sar>
- [36] N. Otsu, "A threshold selection method from gray-level histograms," *IEEE Transactions on Systems, Man, and Cybernetics*, vol. 9, no. 1, pp. 62–66, 1979.
- [37] J. Kittler and J. Illingworth, "Minimum error thresholding," *Pattern Recognition*, vol. 19, no. 1, pp. 41–47, 1986.
- [38] R. D. Johnson and E. S. Kasischke, "Change vector analysis: a technique for the multispectral monitoring of land cover and condition," *International Journal of Remote Sensing*, vol. 19, no. 3, pp. 411–426, 1998.
- [39] A. A. Nielsen, "The regularized iteratively reweighted mad method for change detection in multi- and hyperspectral data," *IEEE Transactions on Image Processing*, vol. 16, no. 2, pp. 463–478, 2007.
- [40] C. Wu, B. Du, and L. Zhang, "Slow feature analysis for change detection in multispectral imagery," *IEEE Transactions on Geoscience and Remote Sensing*, vol. 52, no. 5, pp. 2858–2874, 2014.